Scientia Iranica, Vol. 14, No. 4, pp 336 351

SCIENTIA IRANICA

Large Eddy Simulations of a Mixing Tank with Axial Flow Turbine

P. Zamankhan[1]

An understanding of solid-liquid mixing, with many aspects of mixing, dispersing and contacting, is critical to the efficient preparation of brine from sodium formate and other processes, such as agitated leaching, in the mining industry, rubber crumb, crystallization and precipitations. Generally speaking, solids can be porous catalysts for catalytic reactions, active agents for adsorption, polymers and co-polymers for suspension polymerization or particles that need to be dissolved or coated. In the present attempt, large-eddy simulations of a turbulent flow of a mixture of solid-liquid in a baffled, cylindrical mixing vessel, with a large number of solid particles, were formulated to obtain insight into the fundamental aspects of a solid-liquid mixing. The impeller-induced flow at the blade tip radius of an axial turbine was modeled using the dynamic-mesh Lagrangian method. The simulations were four-way coupled, which implies that both solid-liquid and solid-solid interactions are taken into account. By using a phenomenological model, based on the modified Kelvin-Maxwell model, normal and tangential forces were calculated acting on a particle, due to viscoelastic contacts with other neighboring particles. Simulations were performed for the special case of dissolving solids, whose dissolution rate was assumed to be mass-transfer controlled. The results suggest that the granulated form of dissolving solids, such as sodium formate, may provide a mixture that allows faster and easier preparation of formate brine in a mixing tank.

INTRODUCTION

Mixing processes are widely encountered in chemical, food and mining industries. Stirred tanks are required to fulfill several needs, including the blending of miscible liquids, dispersion of gases or immiscible liquids into a liquid phase, suspension of solid particles, heat and mass transfer enhancements, chemical reactions in industrial processes, such as crystallization operations [1], liquid-liquid extractions [2], biological fermentations [3] and heterogeneous catalytic reactions [4]. Among the various industrial unit operations involved with multi-phase systems, the agitation of solid-liquid systems are commonly encountered in catalytic reactions, leaching and polymerization. Despite their widespread use, complex 3-D recirculation and turbulent flows in the tank usually makes the designing and optimizing of the reactor limited to pilot plant tests and empirical formulation, even for single phase applications.

A number of investigations have been carried out on the fluid dynamic properties of solid-liquid systems in mixing tanks for achieving empirical information [5]. In addition, attempts with the criteria of suspension include Zwietering [6]. The appropriate choice for the geometry of the tank and impeller type can vary widely, depending on the purpose of the operation to be performed in the mixer. The baffled geometry, as illustrated in Figure 1, has been most extensively used in the preparation of brine from sodium formate. Figure 1a displays a three phase gas-liquid-solid mixing tank, in which the gas-liquid interface is located at $H =$ 260 mm. The solid phase is shown to be deposited at the bottom. Figure 1b depicts the bottom view of the four blade pitched blade turbine with its characteristic dimensions. Figure 1c represents a perspective view of the axial flow impeller with some dimensions. The revolving axis of the impeller is the z-axis.

Traditionally, the problem of the designing and scaling up of mixing tanks has been tackled mainly by means of semi-empirical methods. However, economical losses are huge as a consequence of uncertainties in

1. *Laboratory of Computational Fluid and BioFluid Dynamics, Lappeenranta University of Technology, Lappeenranta, Finland; and School of Energy Engineering, Power and Water University of Technology, P.O. Box 16765-1719, Tehran, I.R. Iran.*

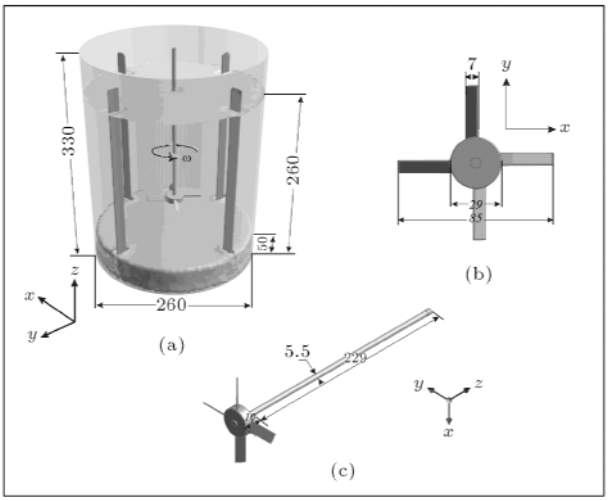

Figure 1. Schematic of a standard baffled tank with an axial flow turbine used in the present attempt. (a) Three phase gas-liquid-solid in the mixing tank. The solid phase is deposited at the bottom; (b) The bottom view of the four blade pitched blade turbine; (c) A perspective view of the axial flow impeller. All dimensions are in milliners.

the design of mixers [7]. It is believed that a significant improvement in mixing tank design can be obtained by developing numerical models that take into account the real flow field inside the vessel. Efforts have been made during the last few years towards the development of predictive methods, based on Computational Fluid Dynamics (CFD), which are capable of providing detailed information on the flow and turbulence fields of mixing tanks [8].

Notice that strong rotations in mixing tanks were observed to considerably change the turbulence dynamics leading to highly anisotropic structuring of turbulent eddies [9]. In this light, advanced modeling techniques, such as Large-Eddy Simulation (LES), would be required in order to predict the flow dynamics in a mixing tank correctly. Recent applications of LES to the hydrodynamic simulation of stirred tanks have been presented in recent articles [10].

Large-Eddy Simulation (LES) is a simulation technique [11] based on the decomposition of the flow field into large and small-scale structures. In this case, large-scale structures are directly simulated in a three-dimensional, time dependent mode, whereas the feed-back effects of small-scale structures are modeled. Notice that accurate experimental data would be required on the mean flow field and on the turbulence characteristics of mixing tanks, to serve as empirical input to predictive models or as validation benchmarks for the computational methods. The flow field can be globally characterized by the power requirement, the pumping capacity of the impeller and the recirculation time through the tank. However, much more detailed information about the mean flow would be needed, in order to improve the design of the equipment or the mixing process. In particular, knowledge of the solid-flow field in mixing tanks is of paramount importance in industrial applications, such as brine-mixing tanks.

The preparation of brine from sodium formate is one of the important applications of solid-liquid mixing. Sodium formate, as illustrated in Figure 2, consists of white hygroscopic crystalline odorless granules and has been widely used to prepare drilling and completion fluids). The solids, as displayed in Figure 2b, are generally added to the surface of the mixing tank. Although the solid density is greater than the liquid density, the solids may initially float and gel with each other. The gel creates a "protective layer" around the solids, making it nearly impossible for the solids inside the gel to be wetted out. However, the granulate form, as shown in Figure 2c, effectively dissolves in a mixing tank. Sodium formate is often used in challenging environments, such as in the Barents Sea. Solutions of sodium formate, including those made from sodium, are used in oilfields as drilling fluids, where fluid viscosity must be low. These fluids are made up of the formate solution itself and water soluble polymers. The fluids are colorless and can be used to drill into the pay zone without threat of plugging or damaging formations.

Sodium formate chemically reduces other components by donating an electron or electrons. Formic acid and oxalic acid are prepared from sodium formate. Sodium formate is used in the manufacture of sodium hydrosulfite, a common reductive bleaching chemical. More applications of sodium formate, such as the recovery of precious metals from acidic effluents, have been discussed in [12]. In addition, sodium formate is used to improve the brightness and color in printing

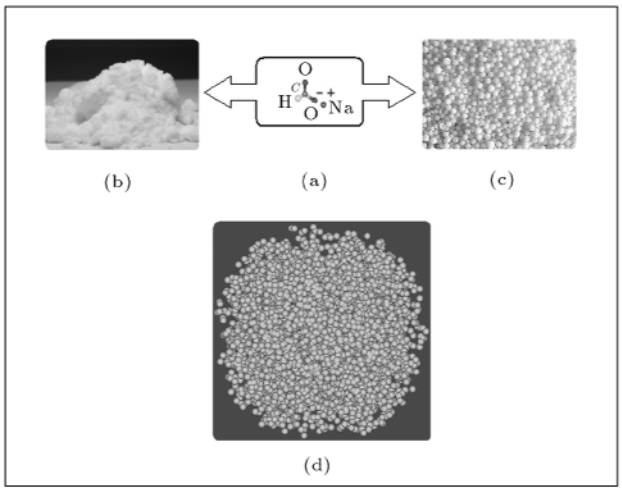

Figure 2. (a) Chemical formula of sodium formate; (b) Sodium formate (white crystal powder); (c) Granular sodium formate; (d) A sample of sodium formate used in the computer simulation reported in the present attempt.

fabrics and paper.

The process using sodium formate powder is a difficult one, because the individual particles of powder can stick together during storage and fuse into a solid mass that is difficult to break up and hydrate in a brine-mixing tank. Limited published data for the solubilities of sodium formate in water include Groscuff [13] and Sidgwick and Gentle [14].

In this paper, the governing equations of the liquid phase with air above (as illustrated schematically in Figure 1a) are solved using a Large Eddy Simulation technique. The particle motion is predicted by a Lagrangian method. Particles are assumed to behave as visco-elastic solids during interactions with their neighboring particles, and inter-particle normal and tangential contact forces between particles are calculated using a generalized Hertzian model [15]. The other forces on a particle that are taken into account are gravitational and drag force, resulting from velocity difference with the surrounding liquid. An Eulerian-Lagrangian type simulation of liquid-particle flow is performed for predicting the flow dynamics of a dense mixture of liquid and particles in a mixing tank.

This attempt may help in overcoming the difficulties which lie in building a comprehensive hydrodynamic theory for the next generation of liquid-solid mixing tanks. Further exploration of a mixing tank requires a different routine, along with the present approach. For example, the continuum approach, as suggested in previous works [16], can be generalized to investigate the dynamics of liquid-particle flows in a mixing tank.

This paper is organized as follows. In the following section, an overview is presented of rotating turbulence, as well as collective processes in liquid-particle flows, useful for developing a simplified model for molecular dynamic type simulations of dense liquid-particle flows. In addition, the developed model is applied to the specific example of a dense liquid-particle mixture under strong rotation in a brain-mixing tank, as illustrated in Figure 1a. Then, the continuum approach is briefly presented, which requires much fewer computational resources for further exploration of brine-mixing tanks. Finally, the concluding remarks are given, which may be of use in creating ideal processing conditions in industrial mixing tanks.

DISCRETE MODELS FOR A MIXING TANK

Turbulence in a steadily rotating fluid, such as that found in brine-mixing tanks, plays an important role in solid dispersion. Figure 3a illustrates the instantaneous velocity vector field in a cutting xz-plane passing through the revolving axis of the impeller of the mixing tank, whose schematic is illustrated in Figure 1a, at the

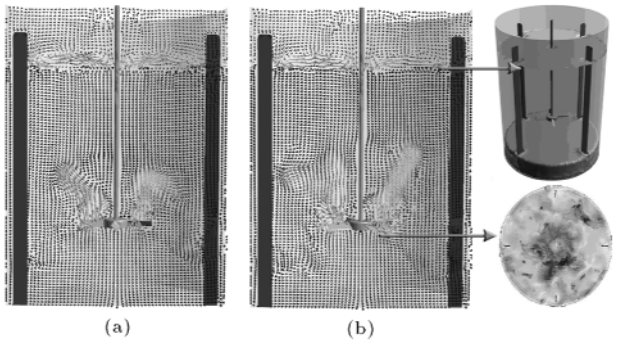

Figure 3. (a) The instantaneous velocity vector field in a cutting xz-plane passing through the revolving axis of the impeller at the Reynolds number of $\mathrm{Re}_{\mathrm{tank}} \approx 110000$; (b) The instantaneous velocity vector field after 0.00175 sec from that in (a). Upper inset: The interface of air and water in the mixing. Lower inset: A high resolution version of the velocity field in a cutting xy-plane located below the impeller.

Reynolds number of $\mathrm{Re}_{\mathrm{tank}} \approx 110000$. Figure 3b shows the instantaneous velocity vector field after 0.00175 sec from that shown in Figure 3a. As illustrated in Figure 3, sufficiently strong rotation is observed to considerably alter the turbulence dynamics, in particular, leading to anisotropic structuring of turbulent eddies. The importance of rotation for the large scales of turbulence is determined by the reciprocal of the turbulent Rossby number, namely $L/u'\omega$. Notice that the Rossby number is the ratio of a rotation time scale to a characteristic time for evolution of the large scales of the turbulence in the absence of rotation.

A large Rossby number represents a case with small effects of rotation. On the one hand, at a sufficiently high Rossby number, the effects of rotation may be neglected altogether. On the other hand, a small enough Rossby number implies strong rotation and, therefore, not enough time for the large scales of turbulence to act on themselves significantly during a rotation period.

Air-Solution Flows

A rotating air-sodium formate solution (which is called "solution" hereafter) system, as illustrated in Figure 1a, may be described using the Volume-Of-Fluid (VOF) technique [17]. This technique provides an excellent approximation when the ratio of liquid to gas densities is large. In the present study, the VOF is used for modeling flows of air and solution as immiscible fluids with interface effects in a brine-mixing tank. Here, the computations are performed on a Cartesian grid, with the interface (between solution and air, in which air can only apply a pressure on solution) being localized by calculating the fraction of each computational cell occupied by one of the two phases. Surface tension effects may be incorporated

by modeling the capillary stresses as the equivalent body force acting in the immediate vicinity of the interface. In this case, an algorithm is required to track the surface as a sharp interface moving through a computational grid.

In the VOF, the velocity of air and solution is considered equal at the interface. In the current attempt, the aim is to combine the best features of the VOF method with those of the LES, in order to achieve more accurate simulations of air-solution flows in a brine-mixing tank.

The filtered continuity, momentum equation for an isothermal air-solution system may be given as:

$$\frac{\partial}{\partial x_i}(\overline{u}_i) = 0, \tag{1}$$

$$\frac{\partial}{\partial t}(p_m \overline{u}_i) + \frac{\partial}{\partial x_i}(\rho_m \overline{u_i u_j}) = \frac{\partial \overline{p}}{\partial x_i} + \frac{\partial \overline{\sigma}_{ij}}{\partial x_j} + \frac{\partial \tau_{ij}}{\partial x_j} \quad \rho_m g \delta_{i3} + F_i^{s\nu}, \tag{2}$$

and:

$$\sigma_{ij} = \frac{2}{3}\mu_m \nu_{m,m}\delta_{ij} + \mu_m \left(\frac{\partial u_i}{\partial x_j} + \frac{\partial u_j}{\partial x_i}\right),$$

is the viscous stress tensor [18]. Here, the unresolved part of $F_i^{s\nu}$ is neglected.

Applying a Gaussian spatial filter, such as:

$$G(x_i \quad \xi_i) = (\gamma/\pi\overline{\Delta}^2)^{1/2} \exp(\quad \gamma |x_i \quad \xi_i|^2/\overline{\Delta}^2),$$

the subgrid scale stress tensor may be modeled as follows:

$$\tau_{ij} = C_{ij} + R_{ij} = \overline{u_i u_j} \quad \overline{\overline{u}_i \overline{u}_j}.$$

Here, $C_{ij} = \overline{\overline{u}_i u'_j} + \overline{\overline{u}_j u'_i}$ represents the interaction between the large and small scales and $R_{ij} = \overline{u'_i u'_j}$ represents the interaction between the subgrid scales.

Note that the $\overline{u}_i \overline{u}_j$ term in Equation 2 requires a second application of the filter. To remedy this further, decomposition is required:

$$\overline{\overline{u}_i \overline{u}_j} = (\overline{\overline{u}_i \overline{u}_j} \quad \overline{u}_i \overline{u}_j) + \overline{u}_i \overline{u}_j = L_{ij} + \overline{u}_i \overline{u}_j. \tag{3}$$

Using Equation 3, the filtered momentum equation may be given as:

$$\frac{\partial \overline{u}_i}{\partial t} + \frac{\partial}{\partial x_j}(\overline{u}_i \overline{u}_j) = \frac{\partial \overline{p}}{\partial x_i} + \nu \frac{\partial}{\partial x_j}\left(\frac{\partial \overline{u}_i}{\partial x_j} + \frac{\partial \overline{u}_j}{\partial x_i}\right) \quad \frac{\partial \breve{\tau}_{ij}}{\partial x_j}, \tag{4}$$

where $\breve{\tau}_{ij} = L_{ij} + C_{ij} + R_{ij} = \overline{u_i u_j} \quad \overline{u}_i \overline{u}_j$.

In order to model the subgrid scale tensor, Menon and Kim [19] suggested that, based on the similarity assumption of a different scale $\tau_{ij} = C_k L_{ij}$, a kinetic energy, k_{test}, can be defined of a test level that includes all energy between two length scales ($\overline{\Delta} < l < \hat{\Delta}$), given as:

$$k_{\text{test}} = \frac{1}{2}(\widehat{\overline{u}}_k \widehat{\overline{u}}_k \quad \widehat{\overline{u}}_k \widehat{\overline{u}}_k). \tag{5}$$

Assuming a similar representation of these two levels, expressions may be obtained for subgrid stress tensor:

$$\tau_{ij} = 2C_\tau \overline{\Delta} k_{sgs}^{1/2} \overline{S}_{ij} + \delta_{ij}/3\tau_{kk}, \tag{6}$$

where $C_\tau = 1/2 L_{ij}\sigma_{ij}/\sigma_{pq}\sigma_{pq}$ and $\sigma_{ij} = \hat{\Delta} k_{\text{test}}^{1/2} \widehat{\overline{S}}_{ij}$. Note that dissipation of energy at the test level takes place between the two length scales and may be expressed as:

$$\varepsilon_{\text{test}} = (\nu + \nu_t)\left(\widehat{\frac{\partial \overline{u}_i}{\partial x_j}}\widehat{\frac{\partial \overline{u}_i}{\partial x_j}} \quad \frac{\partial \widehat{\overline{u}}_i}{\partial x_j}\frac{\partial \widehat{\overline{u}}_i}{\partial x_j}\right) = C_\varepsilon \frac{k_{\text{test}}^{3/2}}{\hat{\Delta}}. \tag{7}$$

Thus:

$$\varepsilon_{\text{SGS}} = C_\varepsilon \frac{k_{\text{test}}^{3/2}}{\overline{\Delta}}.$$

The model of Menon and Kim [19] gives a transport equation for k_{SGS} that uses the local value of C_τ in the diffusion and C_ε in the dissipation term. That is:

$$\frac{\partial k_{\text{SGS}}}{\partial t} + \frac{\partial \overline{u}_i k_{\text{SGS}}}{\partial x_i} = \frac{\partial}{\partial x_i}\left[(C_\tau \overline{\Delta} k_{\text{SGS}}^{1/2} + \nu)\frac{\partial k_{\text{SGS}}}{\partial x_i}\right] + 2\nu \overline{S}_{ij}\overline{S}_{ij} \quad C_\varepsilon \frac{k_{\text{SGS}}^{3/2}}{\overline{\Delta}}, \tag{8}$$

where $\nu_t = C_\tau \overline{\Delta} k_{\text{SGS}}^{1/2}$.

Treating the gas in the tank as incompressible greatly simplifies the analysis. However, a careful treatment of free surface is required to avoid producing any incorrect motion of the surface, since it is assumed to move with the average velocity of air and solution.

Following Chen et al. [20], the density and viscosity in the momentum Equation 2 may be expressed as:

$$\rho_m = \rho_g(1 \quad F) + F\rho_{\text{sol}},$$

$$\mu_m = \mu_g(1 \quad F) + F\mu_{\text{sol}}, \tag{9}$$

where $F(0 \le F \le 1)$ represents the fraction of a control volume occupied by the liquid.

Combining the interface transfer equation in terms of F, namely $\partial F/\partial t + \nu_i F_{,i} = 0$, with continuity (Equation 1), gives:

$$\frac{\partial F}{\partial t} + (\nu_i F)_{,i} = F\nu_{i,i}. \tag{10}$$

Here, the F is used to track the interface instead of a rapid change in density. Note that the unit normal vector for the interface is given by $n_i = F_{,i}/|F_{,i}|$. This scheme results in somewhat sharp interfaces localized in one control volume. However, the interface having surface tension may not be necessarily aligned with logical mesh coordinates. In this light, the interface, in the computational domain, may only be represented as a finite thickness transition region comparable to mesh spacing, through which the liquid volume fraction varies from zero to one.

An expression for the volume form of the surface tension force, $F_i^{S\nu}$, is given by [17]:

$$F_i^{S\nu} = \sigma\kappa\frac{F_{,i}}{[F]}, \tag{11}$$

κ represents the curvature of the interface and is defined as:

$$\kappa = \frac{1}{|F_{,i}|}\left(\frac{F_{,j}}{|F_{,i}|}|F_{,i}|_{,j} \quad F_{,ii}\right).$$

Notice that $F_i^{S\nu}$ is non-zero only within the transition regions, where the liquid volume fraction varies smoothly from zero to one. The square brackets in Equation 11 represent the jump in the value of F across the interface.

The large eddy simulations discussed in this section are performed for a mixing tank, which contains solution with air above, with a four blade pitched blade turbine, as illustrated schematically in Figure 1b. The focus is limited to a case with the Reynolds number of $\mathrm{Re}_{\mathrm{tank}} \approx 110000$. A dynamic-mesh Lagrangian method mesh is used, by which the flow pattern can be calculated without the use of any experimental boundary conditions. No-slip boundary conditions are employed at the impeller blades, the baffles and the tank walls.

The governing equations listed in this section are fully solved, based on a control volume technique. A similar method to that detailed in Chen et al. [20] is implemented for the interface tracking. The sample results, as presented in Figure 3, are obtained using a total number of grid nodes that is more than 8×10^6. Notice that the central differencing scheme is used for spatial discretization and the time is advanced via a second-order implicit scheme.

Particle-Solution Flows

Solid Particles

In general, solid particles, such as those shown in Figure 2c, with mass, m, in a liquid, obey the Langevin equation given as:

$$m\frac{dV_i^p}{dt} = F_i^f + F_i^g + F_i^i + F_i^b. \tag{12}$$

To simplify the equation of motion for the solid particles, it would be useful to define the dimensionless quantities given as below:

$$\mathrm{Re}_p = (1 \quad \phi_s)\frac{d_p|u_i \quad V_i^p|}{\nu_w},$$

$$\mathrm{St} = \frac{2}{9}(1 \quad \phi_s)\left(\frac{\rho_w}{\rho_p}\right)^{1}\frac{d_p|u_i \quad V_i^p|}{\nu_w},$$

$$\mathrm{Fr} = \frac{((1 \quad \phi_s)|u_i \quad V_i^p|)^2}{gL}. \tag{13}$$

The Froude number, Fr, is the ratio of the total kinetic energy of the particle to the gravitational potential. Using the data presented in Table 1, the order of magnitude of dimensionless quantities listed in Equation 13 for the mixing tank, as illustrated in Figure 1, are estimated as $\mathrm{Re}_p \sim 100$, $\mathrm{St} \sim 100$, and $\mathrm{Fr} << 1$. Since the work done by the drag force over the size of particle is much greater than that of thermal energy, the random force, F_i^b, can be neglected. Thus, for the case $\mathrm{Re}_p \sim 100$, and $\mathrm{St} \sim 100$ with nonlinear, visco-elastic, particle-particle interactions, the Langevin equation for translational motion of the jth particle, including buoyancy effects, may be reduced to:

$$\frac{dV_i^j}{dt} = \frac{F_i^D}{m_p} \quad g\left(1 \quad \frac{\rho_{\mathrm{sol}}}{\rho_p}\right)\delta_{iz} + \sum_{p=1}^{N_j} F_{i,jp}^{(n)}, \tag{14}$$

where an expression for the drag force on particles with both the translational and rotational motion, as illustrated in Figure 4a, may be given by [21]:

$$F_i^D = \frac{1}{2}\rho_{\mathrm{sol}}|u_i \quad V_i^P|A\Bigg[C_D(u_i \quad V_i^p) + \varepsilon_{ijk}C_{LR}(u_j \quad V_j^p)\times\frac{\omega_k^R}{|\omega^R|}\Bigg] + F_i^{LG}. \tag{15}$$

Notice that the drag force (Equation 15) includes the lift force due to particle rotational velocity relative to liquid vorticity, which is different from the lift force, due to the velocity gradient.

The effect of the local pressure gradient, as depicted in Figure 4b, gives rise to a force in the direction gradient. In Figure 4b, the two particles on the left are brought into contact by their translational motion. By assuming that the pressure gradient is constant over the volume of the particle, the net pressure force per unit mass acting on the particle may be given as:

$$F_i^p = \quad \frac{1}{\rho_p}\frac{\partial p}{\partial x_i}. \tag{16}$$

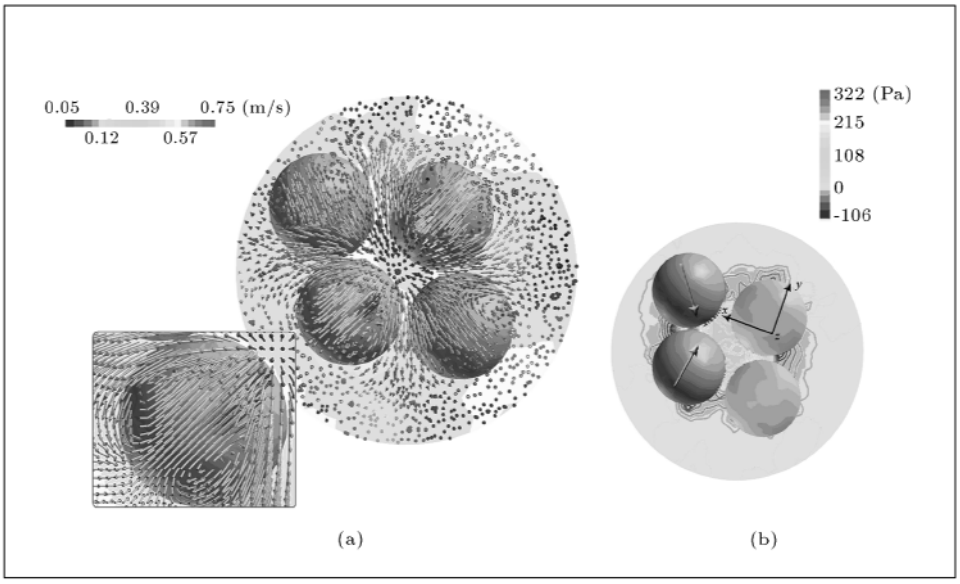

Figure 4. (a) The complex velocity vector field around rotating grains of Sodium Format in a solution. Inset, the velocity vector field around the bottom left particle is magnified to provide a better resolution. Vectors are color-coded by their velocity magnitudes, where the red is for highest velocity and blue represents the lowest; (b) The contours of the pressure around the grains in a mixing tank.

Table 1. Physical and chemical properties of materials used in the simulation.

Material	Properties	Value	
		Reported	**Used in the Model**
Sudium Formate	**Relative Density**	1.258 at 20°C (solution) 1.92 at 20°C (solid phase)	
	Solubility	97 g/100 g water at 20°C	
	Material Type	White, deliquescent, granules or crystalline powder	Spherical particles as illustrated in Figure 2b
	Surface Friction Coefficient	Not reported	0.65 (measured)
	Poisson's Ratio	Not reported	0.244 (assumed)
	Instantaneous Shear Modulus	Not reported	2.53×10^{10} kg/m.s (assumed)
	Long Time Shear Modulus	Not reported	0 kg/m.s (assumed)
	The Relaxation Time	Not reported	9.87×10^{-6} s (assumed)
	Elastic Modulus	Not reported	6.3×10^{10} Pa (assumed)
	Chemical Formula	HCOONa	
	Molecular Weight	68.01	
Water	**Temperature**	20°C	
	Kinematic Viscosity	10^{-6} m^2/s	
	Density	998.2 kg/m^3	
Air	**Temperature**	20°C	
	Kinematic Viscosity	1.5×10^{-5} m^2/s	
	Density	1.2 kg/m^3	
Steel	**Poisson's Ratio**	0.29	
	Elastic Modulus	2.1×10^{11} Pa	
	Density	7890 kg/m^3	

Crowe, Sommerfeld and Tsuji [22] suggested that, if the acceleration of the solid and the liquid phase are of the same order, then, the pressure gradient force is of the order of the acceleration and, therefore, cannot be neglected. Thus, the equation of motion of a particle may be given by:

$$\frac{dV_i^j}{dt} = \frac{F_i^D}{m_p} \quad g\left(1 \quad \frac{\rho_{\rm sol}}{\rho_p}\right)\delta_{iz} \quad \frac{1}{\rho_p}\frac{\partial p}{\partial x_i} + \sum_{p=1}^{N_j} F_{i,jp}^{(n)}. \tag{17}$$

The sodium formate particles have surface roughness on many different length scales. When two particles are brought into contact, the area of contact will only be a fraction of the nominal contact area. The contact regions are small areas, where asperities from one ball are squeezed against those of the other ball. By assuming that the asperities will deform elastically with a finite viscous relaxation time, τ [23], an expression may be obtained for the contact force per unit mass acting on the jth particle, due to contacts between this particle and its neighboring pth particles at time t, given as [15]:

$$F_{i,jp} = \left((E/(3(1 \quad \nu_p^2)m_p))d_p^{1/2}\widehat{\delta}_{jp}^{3/2} + \frac{K_n\tau}{m_p}(G_0^2/(G_0 \quad G_\infty))\widehat{\delta}_{jp}\frac{d\widehat{\delta}_{jp}}{dt}\right)k_{i,jp} \quad (k_t\chi_{jp}^{3/2} + c_t V_{l,jp}^{imp}e_l)e_i, \tag{18}$$

where the deformation of the largest asperities is characterized by $\widehat{\delta}_{jp}$ (which represents overlapping between the pth and jth particles). The surface asperities are responsible for the tangential forces acting between the colliding pairs. The first and second terms on the right hand side of Equation 18 represent the normal and tangential components of the contact force, respectively. Following Silbert et al. [24], the tangential displacement is denoted by χ_{jp}.

In Equation 18, e_i is the tangential unit vector defined as $e_i = \varepsilon_{imq}k_{m,jp}(\varepsilon_{qst}e_{s,jp}^{Vimp}k_{t,jp})$, where $e_{s,jp}^{Vimp}$ represents the unit vector in the direction of the relative impact velocity defined as $e_{s,jp}^{Vimp} = V_{s,jp}^{imp}/|V_{s,jp}^{imp}|$. In this case, the Coulomb friction law describes the friction between two colliding grains, with a surface friction coefficient, μ_p, when there is mutual slipping at the point of contact. The magnitude of χ_{jp}, which represents the tangential displacement, is calculated as necessary to satisfy $|F_{tjp}| = \mu_p|F_{i,njp}k_{i,jp}|$. Otherwise, the contact surfaces are considered as stuck, while $|F_{tjp}| < \mu_p|F_{njp}|$. $|F_{tjp}|$ and $|F_{njp}|$ are the magnitude of the normal and tangential components of the contact force, respectively.

Here, the rate of change of tangential displacement, χ_{jp}, is given by $d\chi_{jp}/dt = V_{i,jp}^{imp}e_i$. The displacement, χ_{jp}, should be set initially to zero when a new contact is established, and, once the contact is broken, all memory of the prior displacement will be lost. As illustrated in Figure 5, frictional forces induce torques on particles. The total torque on particle j may be defined as [15]:

$$T_{i,j} = \quad 1/2\sum_{p=1}^{N}\varepsilon_{iqr}m_j r_{jp}k_{q.jp}F_{r,jp} + 2.01\mu_{\rm sol}d_p^3(1/2\varepsilon_{ijk}\partial u_k/\partial x_j \quad \omega_{i,j}^{(p)})(1 + 0.201\ {\rm Re}_\omega^{1/2}), \tag{19}$$

where ${\rm Re}_\omega = |\omega_{i,j}^{(p)}|d_p^2/\nu_{\rm sol}$. The second term on the left hand side of Equation 2 represents the torque applied to particle j, due to liquid shear stress distribution on the particle surface [22].

Hence, Equation 17 must be augmented by a torque equation for the rotational motion of particle j, which is given as:

$$J_j\frac{d\omega_{i,j}^{(p)}}{dt} = T_{i,j}. \tag{20}$$

Assuming that the apparent surface of contact is built up of a larger number of hierarchically ordered asperities, Brilliantov et al. [25] suggested that the friction coefficient, μ_p, may be expressed in terms of mesoscopic parameters. However, in the present attempt, the friction coefficient is found by comparing the geometry of a dry spill of sodium formate particles observed experimentally and to that obtained using simulations. A detailed description of the method for estimating the coefficient of friction is presented in the following.

To obtain an expression appropriate to spherical particle-flat wall contact from Equation 18, $d_p/2$ has to replace d_p.

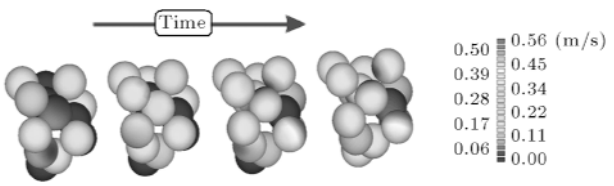

Figure 5. Temporal evolution of the velocity of colliding particles with diameter of $d_p = 5$ mm. The physical properties including the coefficient of friction are reported in Table 1. The particles are color-coded using their velocity magnitudes. Instantaneous configurations are each separated by $t \approx 5 \times 10^{-7}$ sec.

An Estimation of Coefficient of Friction

This section addresses spills of sodium formates onto a flat surface, which collect in a pile. Molecular dynamic type simulation techniques may provide insights into the dynamics of the pile, which are not very well understood. Traditional molecular dynamics analysis relies on the classical Hertzian impact theory and uses particle contacts of finite duration. In this case, a model for collision between particles was used by artificially increasing the duration of a contact between the particles, as suggested by Silbert et al. [24]. However, the disadvantage of the traditional approach is that the softer, normal interactions between the particles have to be assumed. Hence, prediction of the contact network, composed of frictional contacts, by the traditional model, should be considered with caution. By extending the existing formalism, an accurate contact dynamics algorithm is proposed, by which the collective intermittent dynamics found in piles may be captured.

Here, the results of a molecular dynamic type simulation of spills of rough sodium formate, whose physical properties are listed in Table 1, consisting of five hundred and seven mono-sized spherical particles, are presented, using the generalized model discussed in the preceding section. The resulting shape of the spill of beads may be controlled by the distance between the leak and the surface, where the leak collects, and the smoothness of the surface on which the material collects. In this light, the simulation includes the effect of static friction, which is found to be crucial in maintaining a stable spill. Moreover, the diameter of beads are set to $\sigma = 1.5$ mm, which is large enough so that no aggregates can be produced via Van der Waals forces.

As illustrated in Figure 6a, which represents the result of experimentation using rough beads with a diameter of $\sigma = 1.5$ mm, a typical spill exhibits different distinct parts including a rounded shape on top, a linear region characterized by the angle of repose and a tail at the bottom. The straight line in Figure 6a represents the slope of the linear region. In this case, the angle of repose is roughly 33°. The physical properties of particles are found in Table 1. Note that the angle of repose, which is the angle made between the surface and the outside of the cone, achieved in a system, as shown in Figure 6a, seems to be slightly less than the maximum angle of repose produced using, simulation techniques detailed in the preceding section. The ease with which spilled material can move along the collecting surface, may slightly affect the spill geometry.

Figure 6b represents the resulting shape of the spill of beads using simulations, where a static coefficient of friction, $\mu_p = 0.65$, is used. The linear region

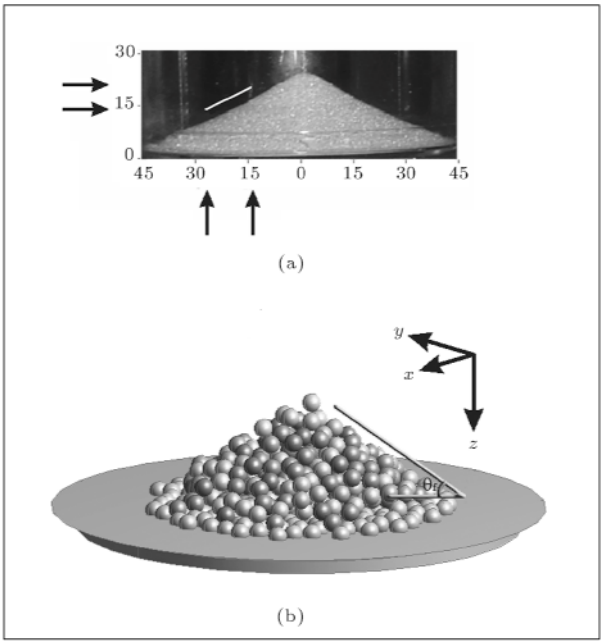

Figure 6. (a) A snapshot of a spill of roughly mono-sized sodium formate granules onto a flat surface. The particle diameter is $d_p \approx 1.5$ mm. The straight line represents the slope of the linear region. In this case, the angle of repose is roughly 33°; (b) An instantaneous configuration of particles slightly before the 507th particle collides in the pile.

characterized by the angle of repose, as depicted in Figure 6a, is satisfactorily reproduced by the model detailed in the preceding section, whose results are shown in Figure 6b. A slightly higher coefficient of static friction has to be used to model the sliding movements of particles over a flat surface made of steel. Here, the coefficient of static friction is set to 0.8 for grain-steel sliding contacts. The base of the flat surface is supported, so that no movement is possible in any direction. The experimental result, as displayed in Figure 6a, is fairly well reproduced by the present model, implying that the correct physical framework has been incorporated.

Solubility

Solubility is the amount of sodium formate that will dissolve in the water. Solubility of sodium formate has special significance in the design of brine-mixing tanks. In this section, a classical particle dissolution rate expression is developed, which will be used to predict particle dissolution rate phenomena in the discrete model detailed in preceding sections. Consider a single grain of sodium formate, which dissolves in the surrounding water, as shown in Figure 7. When there is little sodium formate already in solution, dissolving takes place rapidly. As the solution approaches the point where no sodium formate can be dissolved,

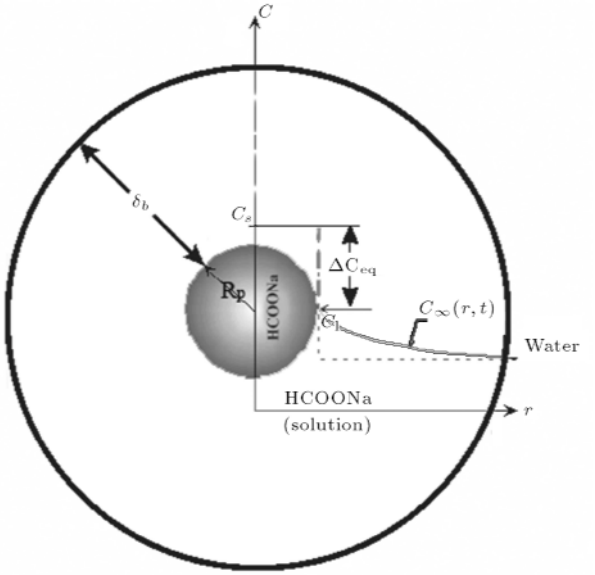

Figure 7. A diffusion model for the dissolution of a single grain of sodium formate in water. Shown are the concentration field within the solid phase, $C_s(r) = C_s =$ constant ($r \leq R_p$), and the concentration jumps across the interface, $\Delta C_{\rm eq} = C_{l0} \quad C_s$, at the solid surface. Note that the solution has lower average concentration of sodium formate, C_∞, than the equilibrium value C_{l0}.

dissolving takes place more slowly. In this case, adding heat is one way to increase solubility.

The goal is to find both the dissolution rate and the concentration profile around a single, stationary grain of sodium formate. The mass balance in spherical coordinates originating from the center of the grain may be given as:

$$\frac{\partial C_l}{\partial t} = \frac{1}{r^2}\left\{\frac{\partial}{\partial r}\left[D_{\rm sol} r^2 \left(\frac{\partial C_l}{\partial r}\right)\right]\right\}. \tag{21}$$

Assuming that the diffusivity, $D_{\rm sol}$, changes insignificantly in the radial direction, Equation 21 reduces to:

$$\frac{\partial C_l}{\partial t} = D_{\rm sol}\left\{\frac{\partial^2 C_l}{\partial r^2} + \frac{2}{r}\left(\frac{\partial C_l}{\partial r}\right)\right\}, \qquad (r > R_p). \tag{22}$$

The solution to this problem, using a spherical transform variable, $u = C_l r$, and then taking the Laplace transform with respect to time, may be given as:

$$C^* = \frac{R_p}{r}{\rm erfc}\left(\frac{(r/R_p) \quad 1}{\sqrt{4D^t_{\rm sol}/R_p}}\right), \qquad (r/R_p \geq 1). \tag{23}$$

The solution (Equation 23) indicates that, at short times, namely; $t << R_p^2/\pi D_{\rm sol}$, an expression for the interfacial flux may be given as $J(t) \cong \sqrt{D_{\rm sol}/\pi t}(C_{l0}$ $C_\infty)$, whereas, at long times, namely $t >> R_p^2/\pi D_{\rm sol}$, it simplifies to a value that depends on the grain size, as given by $J(R_p) \cong D_{\rm sol}(C_{l0} \quad C_\infty)/R_p$. This suggests that using the smaller size grains may increase the interfacial flux.

The interface, as illustrated in Figure 7, moves during the dissolution processes. Note that the position of the interface can be tracked by the interface characteristic, $K_{\rm sphere} = (R_p(t) \quad R_{p0})/\sqrt{4D_{\rm sol}t}$. It is straightforward to obtain the expressions for the characteristic equation:

$$2(K_{\rm sphere})^2\left[1 \quad \sqrt{\pi}K_{\rm sphere}e^{(K_{\rm sphere})^2}{\rm erfc}(K_{\rm sphere})\right] = \quad S, \tag{24}$$

and the interfacial speed given as:

$$\frac{dR_p}{dt} = (K_{\rm sphere}\sqrt{D_{\rm sol}})t^{\quad 1/2} = \frac{\kappa}{\sqrt{t}}. \tag{25}$$

The diffusion layer thickness may be predicted, using the following expression:

$$\frac{\delta_B}{K_{\rm sphere}} = \frac{S}{2(K_{\rm sphere})^2}. \tag{26}$$

As shown in Figure 8, the thickness of the boundary layer decreases with increasing the magnitude of saturation, $|S|$. Note that the ratio between particle size and diffusion layer thickness is an important factor in controlling the shape of the particle dissolution profiles.

The solution concentration, C_∞, increases with time, due to continuous dissolution of sodium formate granules in water. However, the local concentration could be nearly uniform everywhere within the mixing tank, due to perfect stirring induced by the axial flow turbine. In this light, if the kth grain dissolves at the rate of $4\pi J_k(t)R_p^2$, then, the total rate of accumulation of sodium formate in the tank per unit

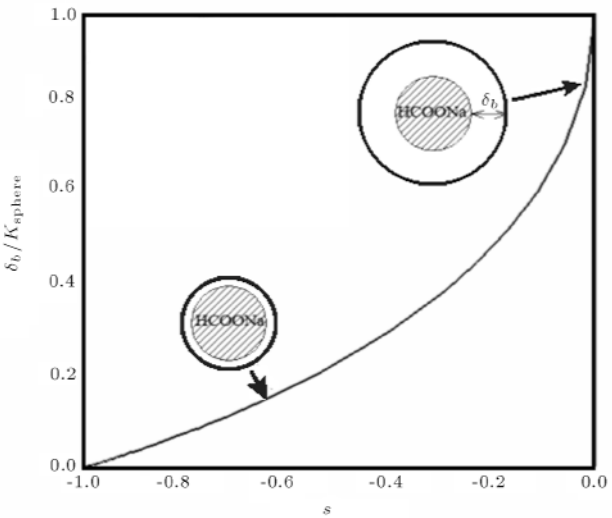

Figure 8. Variations of dimensionless diffusion layer thickness with saturation.

volume is $\sum_{k=1}^{N_p} 4\pi J_k(t) R_p^2 / V_{\text{water}}$. Thus, the average local concentration, $C_\infty(t)$, may be given as:

$$C_\infty(t) = 4\pi / V_{\text{water}} \int_0^t \sum_{k=1}^{N_p} J_k(t') R_k^2 dt'.$$

In actual situations, as illustrated in Figures 9 and 10, the dissolution is not diffusion-controlled and can be complicated by the translational and rotational motion of the particles, as well as particle-particle interactions. In this case, the mass transfer coefficient [26] may be estimated using $Sh = 2kR_p/D_{\text{sol}} = (2(1 \quad \phi_s) + A\text{Re}_p^{\alpha} Sc^{\beta})$. Currently, no information exists for the coefficient of A and power α. However, it is reasonable to assume that $\beta \approx 0.33$ [27]. Note that k characterizes the stirring induced by the movements of the grain, which brings fresh portions of the water in contact with the sodium formate, thereby, increasing the rate of solution.

The simplified diffusion layer model presented in this section provides an approximation for estimating the dissolution rate and the concentration profile around the grain of sodium formate in a brine-mixing tank, as illustrated in Figure 1a.

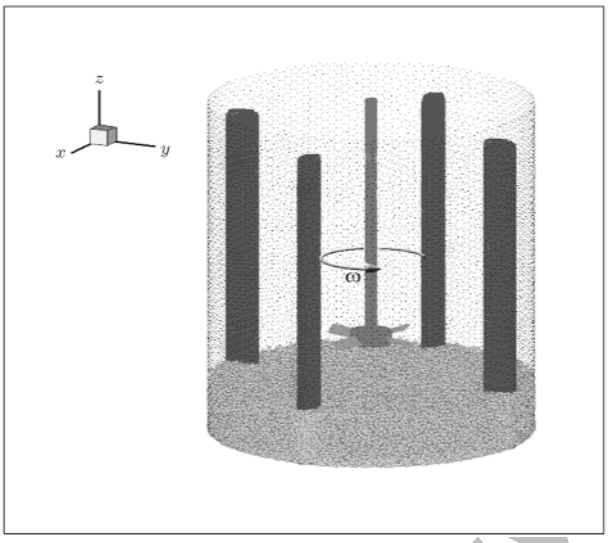

Figure 9. A perspective view of initial configuration of sodium formate grains in the mixing tank. Roughly 2×10^6 monosized particles with diameter of 1.5 mm are used in the simulation.

Liquid Phase

To predict the solution flow field in the mixing tank, a generalized form of the Navier-Stokes equations for the solution interacting with sodium formate granules is used which may be given as:

$$(\rho_{\text{sol}}(1 \quad \phi_s)u_i)_{,i} \quad (\rho_{\text{sol}}(1 \quad \phi_s))_{,t} = 0, \tag{27}$$

$$(\rho_{\text{sol}}(1 \quad \phi_s)u_i)_{,t} + (\rho_{\text{sol}}(1 \quad \phi_s)u_i u_j)_{,j} = ((1 \quad \phi_s)p)_{,i} + ((1 \quad \phi_s)\sigma_{ij})_{,j} (1 \quad \phi_s)\rho_{\text{sol}} g\delta_{iz} + f_i. \tag{28}$$

The last term on the right hand side of Equation 28 represents the particle effect on the solution, which is given as the sum of all hydrodynamic forces on the particles in a computational cell, namely $f_i = 1/(V_c(1 \quad \phi_s)) \sum_{s=1}^{N_c} F_i^D$.

By applying the Gaussian filter $G(x_i \quad \xi_i) = (\overline{\gamma}/\pi\overline{\Delta}^2)^{1/2} \exp(\ \overline{\gamma}|x_i \quad \xi_i|^2/\overline{\Delta}^2)$ with filter width $\Delta_i (i = x, y, z)$ (taken equal to the grid spacing) to Equations 27 and 28, the filtered equations are

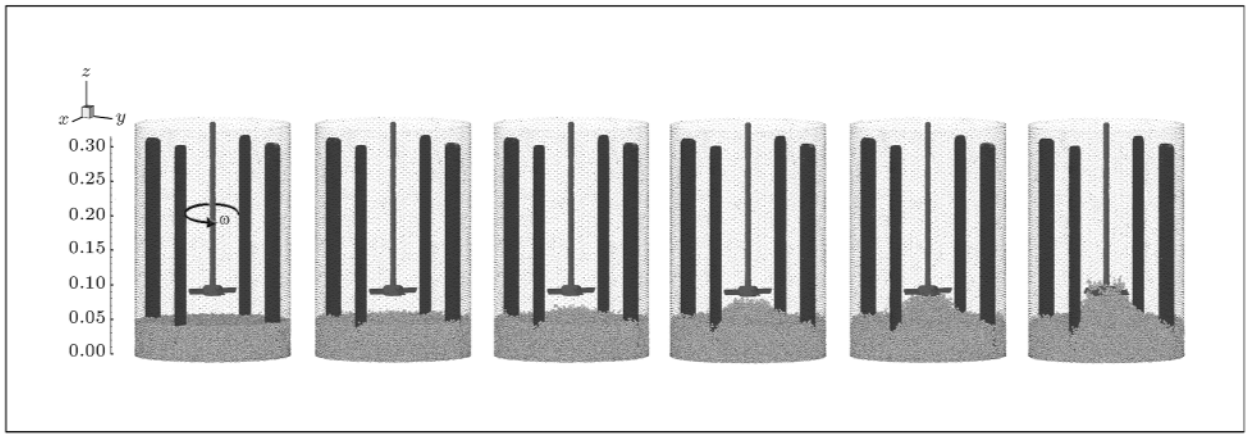

Figure 10. Temporal evolution of position of sodium formate grains in the mixing tank. Roughly 2×10^6 initially monosized particles with diameter of 1.5 mm were used in the simulation. The angular velocity of the axial flow turbine is set at 925 rpm. The instantaneous realizations each separated by roughly 0.25 sec. Movements of particles can be clearly seen.

obtained as follows:

$$(\overline{\rho_{\rm sol}(1 \quad \phi_s)u_i})_{,i} \quad \overline{\rho_{\rm sol}(1 \quad \phi_s)}_{,t} = 0, \tag{29}$$

$$(\overline{\rho_{\rm sol}(1 \quad \phi_s)u_i})_{,t} + (\overline{\rho_{\rm sol}(1 \quad \phi_s)u_iu_j})_{,j} = (\overline{(1 \quad \phi_s)p})_{,i} + (\overline{(1 \quad \phi_s)\sigma_{ij}})_{,j} \quad \overline{(1 \quad \phi_s)}g\rho_{\rm sol}\delta_{iz} + \overline{f}_i. \tag{30}$$

Notice that any quantity, such as u_i in the flow domain, can be decomposed as $u_i = \overline{u}_i + u_i'$, where u_i' is the subgrid-scale part that accounts for the scales not resolved by the computational grid.

Equations 29 and 30 look like the equation of motion of a fluid of variable density, $\rho = \rho_{\rm sol}(1 \quad \phi_s)$. Hence, a Favre filter can be defined as:

$$\widetilde{u}_i = \frac{\overline{\rho u_i}}{\overline{\rho}}. \tag{31}$$

This gives rise to the alternative decomposition, $u_i = \widetilde{u}_i + u_i''$, where u_i'' represents the subgrid-scale part u_i, based on Favre filtering. The Favre filtered governing equations are given as:

$$(\overline{\rho}\widetilde{u}_i)_{,i} \quad \overline{\rho}_{,t} = 0, \tag{32}$$

$$(\overline{\rho}\widetilde{u}_i)_{,t} + (\overline{\rho}\widetilde{u}_i\widetilde{u}_j)_{,j} = \left(\overline{(1 \quad \phi_s)}\widetilde{p}\right)_{,i} + \left(\overline{(1 \quad \phi_s)}\widetilde{\sigma}_{ij}\right)_{,j} + \tau_{ij,j} \quad \overline{\rho}g\delta_{iz} + \overline{f}_i. \tag{33}$$

In Equation 33, the molecular stress tensor and the subgrid scale stress tensor are given as:

$$\sigma_{ij} = \frac{2}{3}\mu_{\rm sol}u_{p,p}\delta_{ij} + \mu_{\rm sol}(u_{i,j} + u_{j,i}), \tag{34}$$

$$\tau_{ij} = \overline{\rho}\left(\widetilde{\widetilde{u}_i\widetilde{u}_j} \quad \widetilde{u}_i\widetilde{u}_j + \widetilde{u_i''\widetilde{u}_j} + \widetilde{\widetilde{u}_iu_j''} + \widetilde{u_i''u_j''}\right). \tag{35}$$

As a tentative first attempt at closure, the LES equations, Equations 32 and 33, may be closed with a subgrid-scale model for τ_{ij} given as [28]:

$$\tau_{ij} = \overline{\rho}(\widetilde{\widetilde{u}_i\widetilde{u}_j} \quad \widetilde{\widetilde{u}}_i\widetilde{\widetilde{u}}_j) + 2C_1\overline{\rho}\Delta_i^2(\widetilde{S}_{mn}\widetilde{S}_{mn})^{1/2}\left(\widetilde{S}_{ij} \quad \frac{1}{3}\widetilde{S}_{pp}\delta_{ij}\right) \quad \frac{2}{3}C_2\overline{\rho}\Delta_i^2(\widetilde{S}_{mn}\widetilde{S}_{mn})^{\frac{1}{2}}\delta_{ij}, \tag{36}$$

where C_1 and C_2 are dimensionless constants, whose values may be determined by correlating the results of analysis, such as that detailed in an earlier work [16]. However, a highly resolved flow field is required to estimate the aforementioned constant accurately. Note that Speziale et al. [28] have found that the values of constants C_1 and C_2 for compressible turbulence are 0.012 and 0.0066, respectively.

The subgrid-scale model (Equaiton 36) was originally proposed for compressible turbulent flow. In the present study, the model (Equaiton 36) is tested to clarify its relevance for dense water-sodium formate flows in the mixing tank, as illustrated in Figure 1, for which the fluctuating fields might not be small compared with those of the mean fields.

Sample Results

By performing the simulations based on the discrete model outlined in the preceding sections (which contains only a few empirical parameters), an increased understanding of the dynamics of dense liquid-particle flows may be obtained in a mixing tank. Here, the main goal is to address problems such as caking in a brine-mixing tank.

The system, as illustrated schematically in Figure 1, represents a virtual type of brine-mixing tank. The simulation is performed using pure water with air above in a cylindrical mixing vessel. An axial flow turbine is located in the center of the vessel, as shown in Figure 1a. The rotor and impellers are made of steel, whose physical properties as an elastic material, are presented in Table 1. The flow is driven by the rotational motion of the axial flow turbine in a xy-plane, given as $\boldsymbol{\omega} = \omega e_z$.

The particle dynamic type simulation is performed to calculate the motion of particles in the liquid. The contact force, as described in the preceding section, is used to capture the major features of grain interaction. A particle dynamic model is employed to account for particle contacts of finite duration, in which the viscoelastic behavior of the particles is represented using a nonlinear Hertzian type model, as presented in the preceding section. Note that the use of a nonlinear viscoelastic model is essential for capturing granular structure formation and caking phenomenon in the mixing tank.

Roughly 2×10^6 identical, slightly overlapping, spherical sodium formate particles with an initial diameter of $d_{p0} = 1.5$ mm are used to fill the tank, as illustrated in Figure 1a. The initial configuration of sodium formate particles in the tank is illustrated in Figure 9a. The free surface, which was a heap type before mixing began, was located at $h_0^* = h_0/d_p \approx 35$.

Equations 17 and 20 are integrated using 4th and 5th order embedded formulas from Dormand and Prince [29], with $\Delta t = 5 \times 10^{\ 8}$ s. The calculation of drag force acting on a particle requires knowledge of the local averaged values of the fluid velocity components at the position of the particle in the Lagrangian grid. Due to the numerical solution method detailed

below, these variables are only known at discrete nodes in the domain. Hence, a mass weighted averaging technique [30] has to be employed for calculating the averaged quantities in the Lagrangian grid.

The solution of the gas field requires the computational domain, as depicted in Figure 9, to be divided into cells. The calculation of the gas is based on the numerical solution of the set of partial differential Equations 32, 33 and 36. The flow is resolved using 5×10^5 tetrahedral cells. The mesh-spacing of this grid should be larger than the particle diameter. The solutions of Equations 32 and 33 require specification of the solids fraction at the appropriate grid nodes. The value of the solids fraction is obtained from particle dynamic simulations by counting the volume of particles within each computational cell divided by the volume of the cell. The linear interpolation routines are used to communicate the information from grid-nodes to particle positions and vice-versa.

The governing equations are fully solved with a second-order finite volume method on a staggered grid, where the time is advanced via a second-order implicit scheme. The time step for the liquid phase equals 10^{-5} s. The grain size shrinks with time, due to the dissolution of sodium formate in the water. Using the diffusion layer model presented in the preceding section, the particles shrink with different dissolution rates. Here, the Sherwood number is estimated as $\mathrm{Sh} = [2(1 \quad \phi_s) + 0.86\ \mathrm{Re}_p^{0.55} Sc^{0.33}]$ using the LES technique, whose sample results are presented in Figure 4. The new particle size is calculated every 5×10^{-4} s.

Notice that it is assumed that the shape of the grains is always spherical, as illustrated in Figure 10. In actual situations, it is likely that the particles become non-spherical, for which no reliable expression exists for drag force, such as that presented in Equation 15. These complexities are neglected at this stage.

The collision time of fine particles, as illustrated in Figure 11, having small impact velocity, could be significantly large, which may even be in the order of 10^{-3} sec. This observation suggests that, by adding the adhesive force between sodium formate grains, the collision becomes completely plastic, with no restitution period after the approaching period during a collision. In this light, exceeding a critical size for grains phenomena, such as caking, might be prevented. The results, as illustrated in Figure 12, suggest that a combination of tangential and axial action may guarantee ideal mixing [31].

Notice that the role of the adhesive force between the grains in the development of large solid structures in a brine-mixing tank merits further investigation. It is likely that non-spherical structures will form in actual situations. These complexities are neglected at this stage.

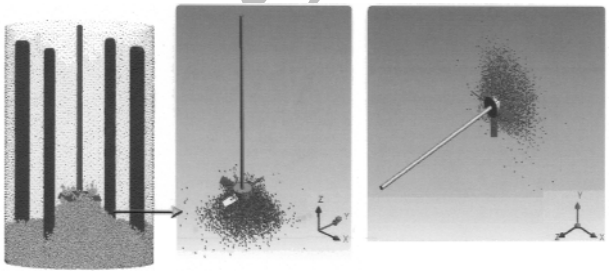

Figure 11. Different views of an instantaneous configuration of the sodium formate particles after nearly $t \approx 2$ sec of simulation in which the rotation speed of the four blade pitched blade turbine is set to $\omega = 925$ rpm. In the insets, only about 5000 particles are shown.

Fluid Structure Interaction

Mixing processes in a mixing tank appear to be of an interdisciplinary nature, comprising those physical phenomena which involve significant mutual interaction among hydrodynamics and structural forces. The problem involves significant nonlinearities and viscous effects, but, nothing that could be termed a systematic theory has been developed to date.

The advantage of the proposed approach is that issues such as Fluid-Structure Interaction occurring in the mixing tanks, can be investigated. Figure 13a illustrates the velocity field at the rotation speed of the turbine of $\omega = 250$ rpm. As can be seen from Figure 13a, the flow of a solution-particle mixture at sufficiently strong rotation may lead to the anisotropic structuring of turbulent eddies. This may cause elastic deformation of the impeller, as depicted in Figure 13c. The deformation of the rotor, in turn, could change the boundary condition of the fluid problem significantly. Using an approach outlined in [32], the deformation of the rotor and blades of the axial flow turbine in a mixing tank can be predicted. In this case, the analysis should provide a strong coupling between the

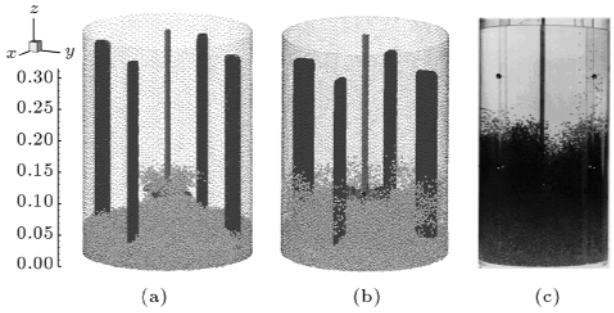

Figure 12. Tank with mixing turbine. (a) An instantaneous configuration of solid particles in a high speed axial flow turbine; (b) A typical configuration of solid particles around the Ruston turbine which rotates at $\omega = 400$ rpm [31]; (c) Combination of tangential and axial action that guarantees ideal mixing.

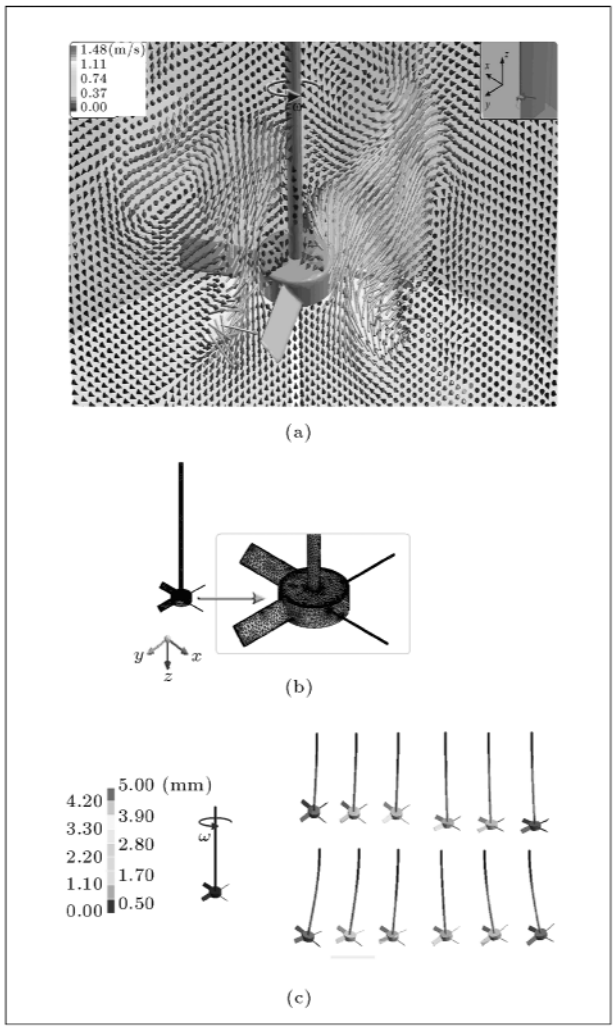

Figure 13. (a) The instantaneous velocity vector field in a cutting xz- and yz-planes passing through the revolving axis of the impeller of the mixing tank; (b) A finite element grid for the rotor and blades; (c) Deformations of the elastic rotor caused by rotating liquid-particle system. The rotor and blades are color-coded using the local displacement magnitude where the red color represents significant displacement as large as 5.0 mm.

dynamics of liquid-particle flow and the dynamics of structures. Using a finite volume approach for the axial flow turbine [32], a coupled system is developed, in which the interaction forces between fluid and structure are accounted for and the resultant motions of the rotor are predicted, as illustrated in Figure 13c.

Presently, no details, such as the flow dynamics of sodium formate grains in a mixing tank at different rates of rotation of the turbine, can be provided, using even the simplified approach described above. Limitations in the available computational resources urge using an alternative approach, such as a continuum approach, which has been proposed in an earlier work [16]. Indeed, the discrete model developed in this paper provides substantial insight into the physics of a mixing tank, which could lead to improved constitutive equations for continuum models.

SAMPLE RESULTS OF CONTINUUM MODEL

Further exploration of a mixing tank requires a different routine, along with the present approach. To this end, the approach suggested in [16] is generalized to investigate the dynamics of liquid-particle flows in a mixing tank. The results presented in this section suggest that the continuum model retains the essential features that characterize the liquid-particles flows. Impressions of the distribution of solid particles for a mixing tank, as illustrated in Figure 1, are given in Figure 14. The free surface of the sodium formate, as depicted in Figure 9, located at $h^* \approx 35$, was nearly flat before mixing began. Solid concentration, as predicted by the model after $t = 2$ sec of continuum type Eulerian-Eulerian simulation, is depicted in Figure 14b. In this case, the initial solids fraction is set to $\phi_s = 0.55$ and the rate of rotation of the axial flow turbine is $\omega = 925$ in the z-direction. The particle size is 1.5 mm. No dissolution model is used in the continuum model. As can be seen from Figure 14b, the results of the continuum model compare favorably with those obtained by molecular dynamic simulation, as illustrated in Figure 14a. More results will be presented in the sequel to this paper, in which the details of a continuum approach for liquid-particle flows will be discussed.

CONCLUSIONS

A generalized model was build for reliable and accurate predictions of complex, multi-phase processes. The use of a model was presented in investigating the dissolution of sodium formate grains in a mixing tank with an axial flow turbine. A detailed overview has been provided of processes in liquid-particle flows to

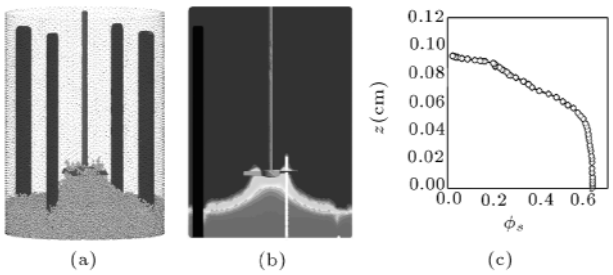

Figure 14. (a) An instantaneous configuration of grains taken from Figure 11; (b) Sample results of continuum model for the distribution of solid volume fraction in the mixing tank in a cutting yz-plane taken after 2 sec; (c) The profile of solid volume fraction along the thick solid line as shown in (b).

obtain insight into the hydrodynamics of a mixing tank and to arrive at a simplified but realistic model for a mixing tank. The simplified model includes an equation of motion for spherical sodium formate particles having repulsive and dissipative interactions with its neighbors. In addition, the liquid-particle interactions are taken into account, using an empirical formula for drag force exerted by the liquid on the particles. In addition, the simplified diffusion layer model is presented, in order to estimate the dissolution rate and the concentration profile around a grain of sodium formate in a brine-mixing tank.

The model is tested through its application to describe the origin of phenomena, such as caking. While progress on the computational and theoretical fronts has been encouraging, there are still many many open problems, including the missing physical properties in Table 1. In addition, the exact role of the adhesive force in the development of large structures in a mixing tank merits further investigation. Note that, due to limitations in available computational resources, neither current details, such as the flow dynamics of sodium formate grains in a mixer with different rotational rates of the impeller, nor the influence of particle size on the dissolution of sodium formate, can be provided.

Limitations, as mentioned above, in available computational resources, urge that further exploration of a mixing tank requires a different routine, along with the present approach. To this end, in the sequel to this paper, as an alternative approach, a continuum approach will be proposed, which retains the essential features that characterize the liquid-particle flows. This attempt might help in overcoming the difficulties which lie in building a comprehensive hydrodynamic theory for the next generation of mixing tanks.

Future plans also include further research into a micro-level mixing topic, which deals with liquid-solid (solid-liquid) mass transfer across a phase boundary. The problem deals more with the rate of the mass transfer and less with the physical distribution of the solids. Notice that the solids can be porous catalysts for catalytic reactions, active agents for adsorption, polymers and co-polymers for suspension polymerization, or particles that need to be dissolved or coated.

NOMENCLATURE

A	projected area of particle
C_{ij}	interaction between large and small scales
C_{LR}	lift coefficient due to particle rotation
C_l	concentration of sodium formate within the boundary layer defined as $\rho_{\mathrm{ISF}}\phi_{\mathrm{SF}} + \rho_w(1 \quad \phi_{\mathrm{SF}})$
C_{l0}	concentration of sodium formate at the solid surface
C_s	concentration within the solid phase
C_∞	average concentration of sodium formate defined as $\rho_{\mathrm{ISF}}\phi_{\mathrm{SF}\infty} + \rho_w(1 \quad \phi_{\mathrm{SF}\infty})$
D	impeller diameter
D_{sol}	coefficient of diffusivity of sodium formate (liquid) in water
d_p	particle diameter
d_{p0}	initial diameter of particle
E	Young modulus
e_i	tangential unit vector
$e_{s,jp}^{\mathrm{Vimp}}$	unit vector in the direction of relative impact velocity
e_l	unit vector used in Equation 16
F	fraction of a control volume occupied by the liquid
F_i^b	Brownian force due to thermal motion of the water
F_i^D	drag force
F_i^F	drag force from fluid
F_i^g	gravitational force
F_i^i	force due to particle-particle interaction
$F_i^{s\nu}$	volume form of the surface tension
F_{LG}	lift force due to velocity gradient
g	acceleration due to the gravity
G_0	instantaneous (glassy) shear modulus
G_∞	long time shear modulus
H	tank height
h	height
J	moment of inertia of particle j
$J(t)$	interfacial flux
K_n	coefficient characterizing the viscous behavior of the grains, as given in Table 1
k_t	elastic modulus in a tangential direction used in Equation 16
k_{test}	kinetic energy
K_{sphere}	interface characteristic defined as $R(t) \quad R_0/\sqrt{4D_{\mathrm{eff}}^t}$
L	linear size of the tank
L_{ij}	interactions among the large scales
m_p	particle mass
N	revolution frequency of the impeller

N_c number of particles in the cell
N_j number of neighboring particles in contact with the jth particle at time t
p pressure
R distance from the axis of rotation
R_{ij} interaction between the subgrid scales
r distance from center of particle
R_p particle radius
S dimensionless saturation defined as $(C_l \quad C_\infty)/(C_l \quad C_S)$
$T_{i,j}$ torque on particle j
u_i liquid velocity
$V_{\rm water}$ volume of water in tank
V_i^p particle velocity
V_c volume of a computational cell

Greek

κ parameter as defined in Equation 25
ε_{ijk} alternating tensor
ϕ_s solid volume fraction of sodium formate (solid phase)
$\phi_{\rm SF}$ volume fraction of sodium formate (liquid phase) around a grain
$\phi_{\rm SF\infty}$ volume fraction of sodium formate (liquid phase) in mixing tank
ω_i rotational velocity of particles
ω angular velocity of rotation of impellers
ω_R particle rotational velocity relative to liquid vorticity
τ relaxation time as given in Table 1
τ_{ij} subgrid scale tensor
σ surface tension coefficient
σ_{ij} viscous stress tensor
ν_w kinematic viscosity of the liquid
ν_p Poisson's ratio
ρ apparent density
ρ_g gas density
ρ_m mixture density
ρ_p material density of the grains
ρ_w water density
$\rho_{\rm sol}$ solution density
$\rho_{\rm ISF}$ sodium formate (liquid phase) density
δ_{ij} Kronecker delta
$\hat{\delta}_{jp}$ deformation of largest asperities (represents overlapping between the pth and jth particles)
$\delta_{\rm BL}$ diffusion boundary layer
χ_{jp} tangential displacement
μ_g gas viscosity
μ_m mixture viscosity
$\mu_{\rm sol}$ solution viscosity
μ_p surface friction coefficient

Superscript

overbar spatial filter

Dimensionless Number and Parameters

Fr Froude number defined as $((1 \quad \phi_s)|u_i \quad V_i^p|)^2/gL$
$\mathrm{Re}_{\rm tank}$ tank Reynolds number defined as ND^2/ν_w
Re particle Reynolds number defined as $(1 \quad \phi_s)d_p|u_i \quad V_i^p|/\nu_w$
RO Rossby number defined as $L/u'\omega$
St Stokes number as defined in Equation 13
Sc Schmidt number $V/D_{\rm sol}$
C_D drag coefficient $24/\mathrm{Re}_p(1+0.15\mathrm{Re}_p^{0.687})$
C^* dimensionless concentration
h^* dimensionless height defined as h/H
h_0^* initial dimensionless height of sodium formate in the tank

REFERENCES

1. Mersmann, A., *Crystallization Technology Handbook*, 2nd Ed., Marcel Dekker, New York, USA (2001).
2. Armenante, P.M. and Tsai, D. "Agitation requirements for complete dispersion of emulsion", presented at *the AICHE Annual Meeting*, Washington, DC, USA (Nov. 1988).
3. Bryant, J., *Adv. Biochem. Eng.*, **5**, pp 101-123 (1977).
4. Baldyga, J. and Bourne, J.R., *Chem. Eng. Commun.*, **28**, pp 231-278 (1984).
5. Baldi, G., Conti, R. and Gianetto, A., *AICHE J.*, **27**, pp 1017-1020 (1981).
6. Zwietering, T.N., *Chem. Eng. Sci.*, **8**, pp 244-253 (1958).
7. Tatterson, G.B., *Scaleup and Design of Industrial Mixing Processes*, McGraw-Hill, New York, USA (1994).
8. Paul, E.L., Atiemo-Obeng, V.A. and Kresta, S.M. (Editors), *Handbook of Industrial Mixing: Science and Practice*, John Wiley & Sons, New Jersey, USA (2004).
9. Jean, M. and Julian, S., *An Introduction to Turbulent Flow*, Cambridge University Press, USA (2000).
10. Derksen, J. and Van den Akker, H.E.A., *AICHE. J.*, **45**(2), pp 209-221 (1999); Moin, P., *International Journal of Heat and Fluid Flow*, **23**, pp 710-720 (2002).
11. Pope, B.S.B., *Turbulent Flow*, Cambridge University Press, Cambridge, UK (2000).

12. Julsing, H.G. and McCrindle, R.I., *Water Science & Technology*, **42**, pp 63-69 (2000).
13. Groschuff, E., *Ber Dtsch. Chem. Ges.*, **36**, p 1783, (1903).
14. Sidgwick, N.V. and Gentle, J.A.H.R., *J. Chem. Soc.*, **121**, p 1837 (1922).
15. Zamankhan, P. and Bordbar, M.H., *J. Applied Mech.*, (T-ASME), **73**, p 648 (2006); Zamankhan, P. and Huang, J., *J. Applied Mech.*, (T-ASME), **74**(4), pp 691-702 (2007).
16. Bordbar, M.H. and Zamankhan, P., *Communications in Nonlinear Science and Numerical Simulation*, **12**, p 254 (2007); Bordbar, M.H. and Zamankhan, P., *Communications in Nonlinear Science and Numerical Simulation*, **12**, p 273 (2007).
17. Hirt, C.W. and Nichols, B.D., *J. Comp. Phys.*, **39**, p 201 (1981).
18. Magnaudet, J. and Eames, I., *Annu. Rev. Fluid Mech.*, **32**, pp 659-708 (2000).
19. Menon, S., Kim, W.W. "High Reynolds number flow simulations using the localized dynamic subgrid-scale model", *34th Aerospace Science Meeting, AIAA* Paper 96-0425, Reno (1996).
20. Chen, L., Garimella, S.V., Reizes, J.A. and Leonardi, E., *J. Fluid Mech.*, **387**, p 61 (1999).
21. Yamamoto, Y., Potthoff, M., Tanaka, T., Kajishima, T. and Tsuji, Y., *J. Fluid Mech.*, **442**, pp 303-334 (2001).
22. Crowe, C., Sommerfeld, M. and Tsuji, Y., *Multiphase Flows with Droplets and Particles*, CRC Press, Boca Raton, Florida, USA (1998).
23. Phan-Thien, N., *Understanding Viscoelasticity*, Springer, Heidelberg, Germany (2002).
24. Silbert, L.E., Ertas, D., Grest, G.S., Hasley, T.S., Levin, D. and Plimpton, S.J., *Phys. Rev. E*, **64**, 051302 (2001).
25. Brilliantov, N.V., Spahn, F. and Hertzsch, J.M., *Phys. Rev. E*, **53**(5), pp 5382-5392 (1996).
26. Zamankhan, P., Malinen, P. and Lepomäki, H., *AICHE J.*, **43**(7), p 1684 (1997).
27. Cussler, E.L., *Diffusion Mass Transfer in Fluid Systems*, Cambridge University Press, New York, USA (1997).
28. Speziale, C.G., Erlebacher, G., Zang, T.A. and Hussaini, M.Y., *Phys. Fluids*, **31**, p 940 (1988).
29. Dormand, J.R. and Prince, P.J., *J. Comp. Appl. Math.*, **6**, p 19 (1980).
30. Zamankhan, P., *Phys. Rev. E*, **52**, p 4877 (1995).
31. Zamankhan, P., Huang, J. and Mousavi, S.M., *Offshore Mechanics and Arctic Engineering (T-ASME)*, in press (2007).
32. Jafari, A., Zamankhan, P., Mousavi, S.M. and Hentinen, K., *J. Applied Phys.*, **100**, 034901 (2006).